Organ-focused mutual information for nonrigid multimodal registration of liver CT and Gd–EOB–DTPA-enhanced MRI

Laura Fernandez-de-Manuel Gert Wollny Jan Kybic Daniel Jimenez-Carretero Jose M. Tellado Enrique Ramon Manuel Desco Andres Santos Javier Pascau Maria J. Ledesma-Carbayo

A B S T R A C T

Accurate detection of liver lesions is of great importance in hepatic surgery planning. Recent studies have shown that the detection rate of liver lesions is significantly higher in gadoxetic acid-enhanced magnetic resonance imaging (Gd–EOB–DTPA-enhanced MRI) than in contrast-enhanced portal-phase computed tomography (CT); however, the latter remains essential because of its high specificity, good performance in estimating liver volumes and better vessel visibility. To characterize liver lesions using both the above image modalities, we propose a multimodal nonrigid registration framework using organ-focused mutual information (OF-MI). This proposal tries to improve mutual information (MI) based registration by adding spatial information, benefiting from the availability of expert liver segmentation in clinical protocols. The incorporation of an additional information channel containing liver segmentation information was studied. A dataset of real clinical images and simulated images was used in the validation process. A Gd–EOB–DTPA-enhanced MRI simulation framework is presented. To evaluate results, warping index errors were calculated for the simulated data, and landmark-based and surface-based errors were calculated for the real data. An improvement of the registration accuracy for OF-MI as compared with MI was found for both simulated and real datasets. Statistical significance of the difference was tested and confirmed in the simulated dataset ($p < 0.01$).

1. Introduction

The advances made in recent decades in the understanding of liver anatomy and physiology (Couinaud, 1999), together with the improvement of medical imaging techniques (Handels and Ehrhardt, 2009; Radtke et al., 2007) and the progressive safety of surgical instrumentation, allow surgeons to design complex liver resections more accurately and effectively without jeopardizing patient safety. Further, preoperative planning has become an essential task before undertaking liver surgery. It requires the mapping of hepatic vasculature, spatial localization of tumors and their relation with other tumors or vascular structures, and the estimation of remnant liver volume in order to determine the suitability of a patient for surgery and to decide the procedure. Accurate detection of individual liver lesions is of great importance because their number, location, and relationships determine both resectability (the probability of performing a resection safely) and radicality (the probability of a potential cure by achieving an R0 resection) (Solbiati et al., 1999).

During preoperative planning of a liver resection, different imaging modalities play different roles: for example, for accurate detection of cancer (staging) and for practical description of inner liver anatomy (mapping). Recently, clinical protocols have included contrast-enhanced computed tomography (CT) and a liver-specific contrast agent-enhanced magnetic resonance imaging (MRI). Several studies have analyzed the advantages and constraints of both methods (Oliva and Saini, 2004; Oudkerk et al., 2002; Weinmann et al., 2003). Contrast-enhanced portal-phase CT imaging offers high

sensitivity and specificity for detecting hepatic metastases and is in most cases more convenient than MRI for evaluating the extrahepatic abdomen (Oliva and Saini, 2004) and for estimating remnant liver volumes because of its higher spatial resolution, better vessel visibility, and wide availability and acquisition speed. However, the lesion detection rate has been found to be significantly higher with Gd–EOB–DTPA-enhanced MRI as compared with CT, especially for small lesions (Donati et al., 2010; Hammerstingl et al., 2008) (Fig. 1). Gd–EOB–DTPA (gadoxetic acid, Primovist® in Europe, Eovist® in the US, by Bayer HealthCare Pharmaceuticals) is an organ-specific contrast medium for hepatic MRI, in use since 2005. In delayed T1-weighted MRI, it produces strong signal enhancement in normal liver parenchyma and absence of signal for focal liver lesions with absence of hepatocellular activity. Consequently, detection of liver metastases and other secondary malignant liver tumors is improved. However, vessels are not opacified.

Considering the advantages and disadvantages of the different imaging modalities and contrast media, several researchers have pointed out the importance of combining MRI and CT for the detection and localization of hepatic lesions and their relation with vessels for therapy planning (Bluemke et al., 2000; Kong et al., 2008; Lange et al., 2005a). In this work, we propose a nonrigid registration framework for aligning contrast-enhanced portal-phase CT and delayed T1-weighted Gd–EOB–DTPA-enhanced MRI into a common coordinate system. As far as we know, this problem has never been tackled before. To use all available data and improve the registration robustness and accuracy, we propose the use of an organ-focused mutual information (OF-MI) registration criterion.

1.1. State of the art

To date, commercial systems for planning hepatic surgery mostly align images rigidly. However, registering soft tissues with rigid registration may result in errors as high as 19–20 mm (Archip et al., 2007; Lee et al., 2005), due to deformations that may be caused by liver movements because of respiration, variations of position, and corporal mass changes over time. To improve detection and characterization in terms of volume and relation with vasculature of primary liver cancers (for example hepatocellular carcinoma), secondary tumors (for example, liver metastases secondary to colorectal cancer) and other liver diseases, an accurate multimodal nonrigid image registration algorithm is clearly required.

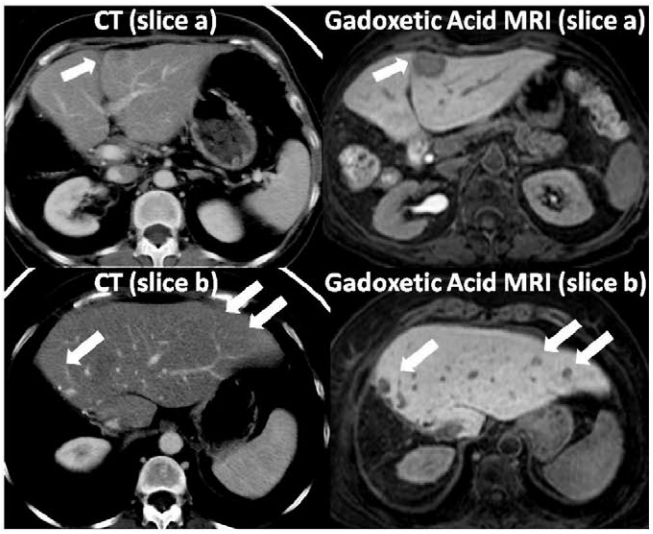

Fig. 1. Contrast-enhanced portal-phase CT image and delayed T1-weighted gadoxetic acid MRI from a patient after right hepatectomy. Arrows show metastases within the different modalities. Each row represents different slice positions. The figure shows how metastases clearly identified in MRI are hardly visible in CT. Better vessel visibility is observed in the CT.

Some studies have presented methods for liver monomodal image registration (Carrillo et al., 2000; Lange et al., 2005b). Other proposed techniques have focused on compensating multimodal image differences in the location and motion of the liver in relation to other organs by using rigid approaches (Van Dalen et al., 2004) or nonrigid methods based on finite elements, B-splines or demons (Archip et al., 2007). Different similitude criteria have been also applied, such as voxel similarity or surface based criteria (Lee et al., 2005). However, to the best of our knowledge, the performance in terms of correspondences between internal liver structures, lesions, and vascular landmarks such as vessel bifurcations has not been evaluated. Additionally, CT/Gd–EOB–DTPA-enhanced MRI registration methods have not been proposed before.

Voxel intensity measures have been shown to be robust measures of image similarity. There are several possible image metrics that are used in voxel similarity-based image registration (Crum et al., 2004; Hill et al., 2001; Maintz and Viergever, 1998; Rueckert and Schnabel, 2011; Zitova and Flusser, 2003): correlation coefficient, sum of squared differences, or mutual information (MI). MI (Maes et al., 1997; Mattes et al., 2003, 2001; Pluim et al., 2003; Wells et al., 1996) is one of the more successful medical image similarity measures. However, extending the maximization of MI to nonrigid image registration and applying it to extensive areas of body images is still an active field of research. Moreover, the most important drawback of MI is that, due to the absence of spatial information, intensity relationships in one region can occasionally mislead the algorithm in another region where the intensity relationships are completely different (e.g., problems with spatially varying intensity inhomogeneity in MRI (Loeckx et al., 2010) or liver vessel misalignments in contrast-enhanced CT and delayed T1-weighted Gd–EOB–DTPA-enhanced MRI (Fig. 2)).

Some studies have focused on improving registration accuracy by considering the use of additional image gradient information (Pluim et al., 2000a,b), neighbor pixel information (Heinrich et al., 2012b; Kybic and Vnučko, 2012; Rueckert et al., 2000), textural information (Heinrich et al., 2012a), or different approaches to weighted MI (Park et al., 2010; Rodriguez-Carranza and Loew, 1999; Van Dalen et al., 2004). One approach to weighted MI is the regularization of MI with the use of weights based on overlaps (Rodriguez-Carranza and Loew, 1999) without including spatial information. Other weighted MI approaches increase histogram contributions of certain pixels (Park et al., 2010) or restrict the registration to certain regions (Van Dalen et al., 2004). Nevertheless, the main problems with the application of the last method are the lack of information on the borders of the regions and neighboring structures, and having too few samples to obtain a good entropy estimation. These problems may be less significant in rigid scenarios. However, they are more relevant when nonrigid transformations are required, hence, the weighted MI performance strongly depends on the concrete registration problem.

Recent approaches add spatial context to mutual information, either by studying different spatial encoding schemes (Zhuang et al., 2011) or by searching for the correspondence of a priori learned set of image patches (Yi and Soatto, 2011). In Hermosillo et al. (2002) the formulation of a locally computed similarity measure is presented and in Rogelj et al. (2003) a variant to obtain pointwise similarity metric is described.

First attempts to incorporate an additional information channel into the histogram definition of the MI were tackled by Studholme et al. (1996) for the rigid registration of MRI and positron emission tomography images of the pelvis. In Studholme et al. (2006) a related method named regional mutual information (RMI) was ap-

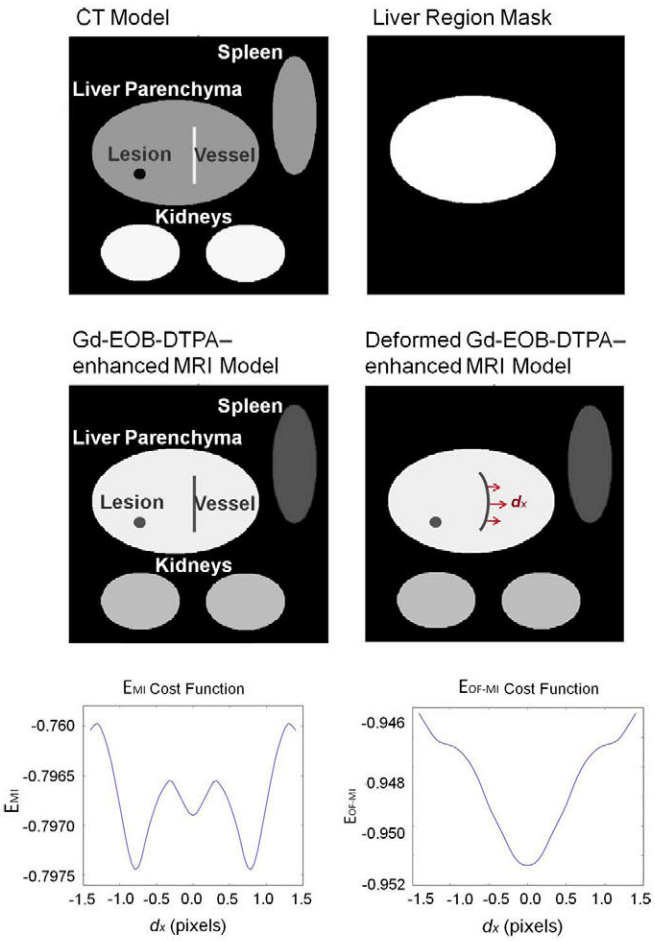

Fig. 2. Cost functions for a synthetic 2D model as a function of horizontal transformation. A local nonrigid deformation is applied with maximum amplitude $\boldsymbol{d}_x$ from −1.5 pixels to 1.5 pixels in the middle of the vessel region. The E_{MI} cost function shows multiple local minima and a global minimum shifted away from 0 where the correct solution should be. The $E_{OF\text{-}MI}$ cost function shows a clean global minimum in the correct location.

plied to analyze local tissue contrast changes in brain MRI nonrigid registration. The RMI was defined as:

$$\mathrm{RMI}(T,R,X) = \mathrm{H}(T) + \mathrm{H}(R) + \mathrm{H}(X) - \mathrm{H}(T,R,X) \tag{1}$$

with X expressing the spatial position of cubic overlapping subregions in the reference image R and the test image T. In Loeckx et al. (2010) a conditional mutual information (cMI) was defined and calculated between two images T, R, given a certain spatial distribution X. Besides the intensity dimensions, a third spatial channel was incorporated into the histogram definition, expressing the spatial location of every joint intensity pair:

$$\mathrm{cMI}(T,R|X) = \mathrm{H}(T|X) + \mathrm{H}(R|X) - \mathrm{H}(T,R|X) \tag{2}$$

In Russakoff et al. (2004), a regional MI was described, introducing neighborhood regions of pixels into a multidimensional histogram. In this work, each pixel co-occurrence was represented by more than one entry in the joint histogram depending on its neighbor pixel co-occurrences. However, one should notice that as described in Russakoff et al. (2004), the main problem in increasing the dimensionality of joint histograms is the need of a higher number of samples to obtain a reasonable estimate of entropy distribution. Therefore, these methods require a large number of image voxels hence increasing the computational complexity enormously. In Russakoff et al. (2004) a method to make the problem more tractable is proposed, taking advantage of the fact that the entropy of a discrete distribution is invariant to rotations and translations and making the simplifying assumption that high-dimensional distributions are approximately normally distributed. In Studholme et al. (1996) preliminary rigid registration results demonstrated the possibility of extending the histogram with a small number of unconnected regions of similar intensity ranges (e.g. air or fat tissue). As the reference image R and the regions L were inherently registered, they proposed an extension I of the mutual information for more than two variables defined by:

$$\mathrm{I}(T,R;L) = \mathrm{H}(R,L) + \mathrm{H}(T) - \mathrm{H}(T,R,L) \tag{3}$$

Their preliminary results motivated us to use the same extension of the mutual information for more than two variables. However, they proposed the use of regions calculated by using only intensity ranges. Unconnected regions containing the same range of intensities were considered as different, which does not allow separating intensity relationships based on anatomical reasons nor having regions with more than one range of intensities.

1.2. Our contribution

As already pointed out above, delayed T1-weighted Gd–EOB–DTPA-enhanced MRI causes strong signal enhancement for normal liver parenchyma. For this reason, the relationship between intensities in CT and MRI images is very different inside and outside the liver. Hence, using the classical formulation of MI, intensity relationships in a region can occasionally mislead the algorithm in another region where the relationships are completely different; especially in nonrigid registrations.

Liver volume estimation from preoperative CT is a routine mandatory process to determine the suitability of a patient for surgery and to make the final clinical decision before extensive hepatectomies (Fernandez-de-Manuel et al., 2011; Heimann et al., 2009). To estimate remnant liver volumes, both manual and automatic segmentation tools are applied in the daily clinical routine. Consequently, liver segmentation from CT images are available in most hospitals for patients considered for liver surgery. For that reason, incorporating the liver segmentation information into the registration process is very feasible.

We discarded the approaches presented in Loeckx et al. (2010), Russakoff et al. (2004) and Studholme et al. (2006) because those techniques cannot take advantage of the available liver segmentations.

In this work, we propose the use of an organ-focused mutual information (OF-MI) criterion. We extend the joint histogram with an additional information channel using an extension of the mutual information for more than two variables similar to the one proposed in Studholme et al. (1996) but with a different probability distribution estimation. Studholme et al. (1996) used regions segmented based on intensity ranges, however, they suggested to exploit a higher level of anatomical knowledge. Therefore, we take advantage of an anatomical segmentation resulting in regions with varying intensities. We consider that using anatomical regions actually allows taking maximum advantage of the definition proposed in Studholme et al. (1996). Additionally, we have extended its implementation to nonrigid multimodal registration. Consequently, our work's main contributions are related to the experimental novelty and the obtained results in a clinical application that benefits from the proposed approach.

Therefore, the main contributions of this work are (1) an organ-focused mutual information as registration criterion that takes advantage of available clinical segmentation, (2) the mathematical formulation for its implementation within a B-spline based registration framework using the explicit derivatives of the metric, (3) a method to simulate Gd–EOB–DTPA-enhanced MRI from CT for validation purposes, (4) a thorough validation of the method with

synthetically generated data as well as its application to relevant clinical liver datasets (CT and Gd–EOB–DTPA-enhanced MRI), and a comparison of the registration performance using OF-MI compared with MI as registration criterion.

The proposed criterion takes into account an organ (liver) segmentation based on the semi-automatic method described in Fernandez-de-Manuel et al. (2009) and Jimenez-Carretero et al. (2011).

The algorithm has been validated and compared with the standard MI on a simulated 3D dataset with 63 image pairs, using a delayed T1-weighted Gd–EOB–DTPA-enhanced MRI simulation framework. Additionally a dataset of seven real subjects referred to surgery with one contrast-enhanced portal-phase CT and one delayed T1-weighted Gd–EOB–DTPA-enhanced MRI each have been used.

2. Methods

In Sections 2.1 and 2.2, we will introduce the general framework and MI, describing briefly the equations presented in previous work (Kybic and Unser, 2003; Thévenaz and Unser, 2000). We will then explain our contribution in Section 2.3.

2.1. Problem definition and registration framework

The intensity-based nonrigid registration algorithm used extends the previous B-spline method of Kybic and Unser (2003). The algorithm determines a set of B-spline coefficients that describe a nonrigid transformation that maximizes an image similarity measure. The transformation model is defined as a linear combination of B-spline basis functions located on a uniform grid. B-spline functions have been widely used to represent deformations (Kybic and Unser, 2003; Ledesma-Carbayo et al., 2005; Oguro et al., 2009; Rueckert et al., 1999; Schnabel et al., 2001), motivated by their compact support, computational simplicity, good approximation properties, and implicit smoothness. We also use B-spline functions for representing continuous images derived from a set of samples (Kybic and Unser, 2003; Thévenaz and Unser, 2000). Moreover, B-spline basis functions are used as Parzen windows (Thévenaz and Unser, 2000) in the similarity criteria, as described later.

The input images are given as two N-dimensional discrete signals: the test image T and the reference image R with intensities $f_t(\mathbf{i})$ and $f_r(\mathbf{i})$, respectively, where $\mathbf{i} \in I \subset \mathbb{Z}^N$, and I is an N-dimensional discrete interval representing the set of all voxel coordinates in the image. For convenience in our formulation we use a continuous representation $f_t^c(\mathbf{x})$ of the discrete test image $f_t(\mathbf{i})$ as follows:

$$\begin{aligned} f_t^c(\mathbf{x}) &= \sum_{\mathbf{i} \in I_a \subset \mathbb{Z}^N} a_{\mathbf{i}} \beta_m(\mathbf{x} - \mathbf{i}) \\ f_t(\mathbf{i}) &= f_t^c(\mathbf{i}) \quad \forall \mathbf{i} \in I \subset \mathbb{Z}^N \end{aligned} \tag{4}$$

where β_m represents an N-dimensional tensor product of centered B-splines of degree m (Kybic, 2001), $a_{\mathbf{i}}$ are the B-spline coefficients that represent the original test image given by its samples $f_t(\mathbf{i})$, and I_a is the set of nodes used to represent the image.

Let $\mathbf{g}(\mathbf{x})$ be a deformation function that finds the spatial correspondence between coordinates in the test and reference images. The deformation is represented using splines:

$$\mathbf{g}(\mathbf{x}) = \mathbf{x} + \sum_{\mathbf{j} \in I_b \subset \mathbb{Z}^N} \mathbf{c}_{\mathbf{j}} \beta_n(\mathbf{x}/\mathbf{h} - \mathbf{j}) \tag{5}$$

described by a finite number of parameters $\mathbf{c} = \{\mathbf{c}_{\mathbf{j}}\}, \mathbf{j} \in I_b \subset \mathbb{Z}^N$; where I_b is an N-dimensional discrete interval representing the set of parameter indexes, $\mathbf{h}$ is the knot spacing on a regular grid over the image, and β_n represents an N-dimensional tensor product of centered B-splines of degree n.

The warped test image W is defined as $f_w(\mathbf{x}) = f_t^c(\mathbf{g}(\mathbf{x}))$. We define the solution to our registration problem as the result of the minimization $\mathbf{g} = \arg\min_{\mathbf{g} \in G} E(\mathbf{g})$, where G is the space of all admissible deformation functions $\mathbf{g}$ and E is the criterion. For the proposed application, we consider the criterion:

$$E(\mathbf{g}) = E_d(W, R) + \gamma E_r(\mathbf{g}) \tag{6}$$

where E_d is an MI-based image dissimilarity criterion and E_r is a regularization term with weight γ used to prevent discontinuities and to guarantee overall smoothness. For this particular problem, we use a discrete approximation to the norm of the Laplacian of the continuous deformation as E_r (Kybic, 2001).

To minimize the criterion E with respect to a finite number of parameters $\mathbf{c}$ we use a gradient descent optimizer with quadratic step size estimation, as recommended in Kybic and Unser (2003). The optimization uses a multiresolution approach for the image model. The multiresolution methodology used creates a pyramid of subsampled images optimal in the L2 sense, taking advantage of the spline representation (Unser et al., 1993). The problem is solved by starting at the coarser level of the pyramid (the most subsampled image) and proceeding to the finest level.

2.2. Mutual information

The joint intensity probability distribution is estimated by means of Parzen windows because of their good properties, such as computational efficiency (Unser, 1999).

Following Thévenaz and Unser (2000), the contribution to the joint histogram of a single pair of pixels with intensities (f_w, f_r) is distributed over several discrete bins (t, r) with t and r belonging to discrete sets of intensities associated with the test and reference images, with ranges from 0 to $n_{binsT} - 1$ and $n_{binsR} - 1$, respectively. Intensities (f_w, f_r) can take values in a continuum in the ranges $(f_{w\,min}, f_{w\,max})$ and $(f_{r\,min}, f_{r\,max})$, respectively. Using B-spline functions of degree m_1 and m_2, the discrete joint probability of co-occurring intensities in the overlap of the two images f_w and f_r is expressed as:

$$p(t, r; \mathbf{c}) = \frac{1}{|I_c|} \sum_{\mathbf{i} \in I_c \subset \mathbb{Z}^N} \beta_{m_1}(t - \tau(\mathbf{i}; \mathbf{c})) \cdot \beta_{m_2}(r - \rho(\mathbf{i})) \tag{7}$$

and the discrete marginal probability distributions for the warped test and the reference images, respectively, are:

$$\begin{aligned} p_T(t; \mathbf{c}) &= \frac{1}{|I_c|} \sum_{\mathbf{i} \in I_c \subset \mathbb{Z}^N} \beta_{m_1}(t - \tau(\mathbf{i}; \mathbf{c})) \\ p_R(r) &= \frac{1}{|I_c|} \sum_{\mathbf{i} \in I_c \subset \mathbb{Z}^N} \beta_{m_2}(r - \rho(\mathbf{i})) \end{aligned} \tag{8}$$

where I_c is a discrete set of samples $I_c \subset I$. τ and ρ are the test and reference images after scaling the continuous interval $(0, n_{binsT} - 1)$ and $(0, n_{binsR} - 1)$, respectively:

$$\begin{aligned} \tau(\mathbf{i}; \mathbf{c}) &= (f_w(\mathbf{i}; \mathbf{c}) - f_{w\,min}) \cdot \frac{n_{binsT} - 1}{f_{w\,max} - f_{w\,min}} \\ \rho(\mathbf{i}) &= (f_r(\mathbf{i}) - f_{r\,min}) \cdot \frac{n_{binsR} - 1}{f_{r\,max} - f_{r\,min}} \end{aligned} \tag{9}$$

The MI-based dissimilarity criterion E_{MI} can be defined from the above probabilities as a function of the deformation parameters $\mathbf{c}$:

$$E_d = E_{MI}(W, R) = -\sum_{\forall t} \sum_{\forall r} p(t, r; \mathbf{c}) \cdot \log \frac{p(t, r; \mathbf{c})}{p_T(t; \mathbf{c}) \cdot p_R(r)} \tag{10}$$

Notice that in this work we denote by E_{MI} the negative version of the standard mutual information, so we search for the E_{MI} minimum.

We can also express MI-based dissimilarity criterion E_{MI} between a warped image W and a reference image R in terms of the marginal and joint entropies:

$$E_{\mathrm{d}} = E_{\mathrm{MI}}(W,R) = \mathrm{H}(W,R) - \mathrm{H}(W) - \mathrm{H}(R) \tag{11}$$

For the optimization algorithm, partial derivatives of the E_{MI} with respect to $\mathbf{c_j}$ are needed:

$$\frac{\partial E_{\mathrm{MI}}}{\partial c_{\mathbf{j},k}} = \sum_{\mathbf{i}\in I_a} \frac{\partial E_{\mathrm{MI}}}{\partial f_w(\mathbf{i})} \cdot \left.\frac{\partial f_t^c(\mathbf{x})}{\partial x_k}\right|_{\mathbf{x}=\mathbf{g}(\mathbf{i})} \cdot \frac{\partial g_k(\mathbf{i})}{\partial c_{\mathbf{j},k}} \tag{12}$$

where k is the dimension of the N-dimensional $\mathbf{c_j}$. For further details on the derivatives calculation, we refer the reader to Thévenaz and Unser (2000).

2.3. Organ-focused mutual information

We present here an OF-MI criterion that allows including probabilities of voxels belonging to the object or the background.

We introduce an additional information channel consisting of an image L containing for every voxel its probability $P_{\Omega_l}(\mathbf{i})$ of belonging to the background Ω_0 and the object (liver) Ω_1, $P_{\Omega_l}(\mathbf{i})$ satisfying $\sum_{\forall l} P_{\Omega_l}(\mathbf{i}) = 1 \forall \mathbf{i}, \quad l = 0, 1$.

Based on (3) (Studholme et al., 1996) we define OF-MI-based dissimilarity criterion $E_{\mathrm{OF\text{-}MI}}$ between a warped image W and a pair (R,L) consisting of a reference image R and the probability image L in terms of the marginal and joint entropies:

$$E_{\mathrm{d}} = E_{\mathrm{OF-MI}}(W,R,L) = \mathrm{H}(W,R,L) - \mathrm{H}(W) - \mathrm{H}(R,L) \tag{13}$$

The joint probability histogram is extended with a third dimension of size 2, with l the coordinate representing inside ($l = 1$) and outside ($l = 0$) the liver region. Using B-spline functions of degree m_1 and m_2, we define a 3D discrete joint probability distribution:

$$p(t,r,l;\mathbf{c}) = \frac{1}{|I_c|} \sum_{\mathbf{i}\in I_c \subset \mathbb{Z}^N} P_{\Omega_l}(\mathbf{i}) \cdot \beta_{m_1}(t - \tau(\mathbf{i};\mathbf{c})) \cdot \beta_{m_2}(r - \rho(\mathbf{i})) \tag{14}$$

The marginal organ-focused joint intensity probability distribution for the reference image is:

$$p_{RL}(r,l) = \frac{1}{|I_c|} \sum_{\mathbf{i}\in I_c \subset \mathbb{Z}^N} P_{\Omega_l}(\mathbf{i}) \cdot \beta_{m_2}(r - \rho(\mathbf{i})) \tag{15}$$

The marginal intensity probability distribution for the test image is given in (8).

The dissimilarity criterion $E_{\mathrm{OF\text{-}MI}}$ is defined from the above probabilities as follows:

$$E_{\mathrm{OF-MI}}(W,R,L) = -\sum_{\forall t}\sum_{\forall r}\sum_{\forall l} p(t,r,l;\mathbf{c}) \cdot \log \frac{p(t,r,l;\mathbf{c})}{p_T(t;\mathbf{c}) \cdot p_{RL}(r,l)} \tag{16}$$

The partial derivatives of the $E_{\mathrm{OF\text{-}MI}}$ with respect to $\mathbf{c_j}$ are:

$$\frac{\partial(E_{\mathrm{OF-MI}})}{\partial c_{\mathbf{j},k}} = \sum_{\mathbf{i}\in I_a} \frac{\partial(E_{\mathrm{OF-MI}})}{\partial f_w(\mathbf{i})} \cdot \left.\frac{\partial f_t^c(\mathbf{x})}{\partial x_k}\right|_{\mathbf{x}=\mathbf{g}(\mathbf{i})} \cdot \frac{\partial g_k(\mathbf{i})}{\partial c_{\mathbf{j},k}} \tag{17}$$

(For further detail on the derivatives calculation, we refer the reader to the Appendix A).

From (13) and (16) the expressions for the marginal and joint entropies remain as follows:

$$\begin{aligned} \mathrm{H}(W,R,L) &= -\sum_{\forall t}\sum_{\forall r}\sum_{\forall l} p(t,r,l;\mathbf{c}) \cdot \log p(t,r,l;\mathbf{c}) \\ \mathrm{H}(W) &= -\sum_{\forall t} p_T(t;\mathbf{c}) \cdot \log p_T(t;\mathbf{c}) \\ \mathrm{H}(R,L) &= -\sum_{\forall r}\sum_{\forall l} p_{RL}(r,l) \cdot \log p_{RL}(r,l) \end{aligned} \tag{18}$$

2.3.1. Estimation of the region probabilities $P_{\Omega_l}(\mathbf{i})$

The probability image L containing $P_{\Omega_l}(\mathbf{i}), l = 0, 1$ is computed from the hepatic masks (liver segmentation) obtained for the surgery planning procedure. Uncertainty of the segmentations could be taken into account by smoothing the mask edges using a Gaussian filtering; however, experiments revealed that this does not bring any benefit for this application. Therefore, in this work, the voxel probability of belonging to a region will be either 0 or 1; as each voxel contributes only to one region.

Considering a binary image $f_\Omega(\mathbf{x})$ with dimensions identical to $f_r(\mathbf{x})$ that represents the clinical segmented liver in the reference image, we define $P_{\Omega_l}(\mathbf{i})$ as follows:

$$P_{\Omega_l}(\mathbf{i}) = \begin{cases} f_\Omega(\mathbf{x})|_{\mathbf{x}=\mathbf{i}} & \text{if } l = 1 \\ 1 - f_\Omega(\mathbf{x})|_{\mathbf{x}=\mathbf{i}} & \text{if } l = 0 \end{cases} \tag{19}$$

In this work the initial liver binary images $f_\Omega(\mathbf{x})$ have been created semi-automatically by a liver segmentation application based on active contours previously described in Fernandez-de-Manuel et al. (2009) and Jimenez-Carretero et al. (2011).

Notice that with our proposed OF-MI we are not neglecting any area of the image, as all the regions are represented in the 3D joint intensity probability distributions and optimized together.

2.3.2. MI versus OF-MI synthetic examples

To illustrate theoretically the behavior of the proposed approach compared with MI and its shortcomings related to its assumption of equal statistical relationships over the whole domain of the images, two 2D basic synthetic images were created representing a contrast-enhanced portal-phase CT model and a delayed T1-weighted Gd–EOB–DTPA-enhanced MRI model. Both models contained the liver, the kidneys, the spleen, and an intrahepatic lesion and vessel. They represented a realistic distribution of intensities and were initially registered completely. We used the CT liver segmentation (liver region mask in Fig. 2). We then applied a mild horizontal nonrigid deformation with maximum amplitude $\boldsymbol{d}_x$ around the center of the hepatic vessel to the Gd–EOB–DTPA-enhanced MRI model and evaluated the dependency of the criterion on $\boldsymbol{d}_x$, with $\boldsymbol{d}_x$ ranging from −1.5 pixels to 1.5 pixels (Fig. 2).

The E_{MI} exhibits multiple local minima and a global minimum far from the correct location. This happens because the intensity relationships between CT and MRI pixels in extrahepatic organs (spleen) mislead the algorithm into considering that the hepatic vessel in MRI should be aligned with the liver tissue in CT. On the other hand, the $E_{\mathrm{OF\text{-}MI}}$ cost function shows a clean global minimum at the correct location, as the intensity relationships inside and outside the liver are considered separately.

3. Validation methodology

In this section, we will first describe the simulated and real image datasets. Then, we will illustrate the definition of the quantitative measures used to validate the experiments. After that, the registration parameters for both, the MI and the OF-MI criteria are given, followed by the validation results.

3.1. Data

3.1.1. Simulated images dataset

A dataset of 63 image pairs, each composed of one simulated hepatic delayed T1-weighted Gd–EOB–DTPA-enhanced MRI and one contrast-enhanced portal-phase CT was generated; the images had different noise levels and deformation values. Gd–EOB–DTPA-enhanced MRI images were simulated from seven real CT images of the abdominal body region at the liver level. CT images were taken as provided. The processing steps to simulate MRI images consisted of a nonlinear intensity transformation, a low-pass Gaussian filter, morphological edge detection, and Gaussian noise addition.

The gray values of the simulated MRI images were calculated by a nonlinear intensity transformation based on intensity distributions of contrast-enhanced portal-phase CT and delayed T1-weighted Gd–EOB–DTPA-enhanced MRI (Fig. 3a and b). By direct observation of these distributions, we assigned the interval of intensities approximating those in MRI to the interval of intensities in the CT for each relevant organ or structure, differentiating between liver structures and background. Therefore, different transformations were applied to different CT regions, assigning tissue-dependent signal intensity to each region (liver and liver background) (Fig. 3c and d). In order to apply these intensity transformations, CT regions were calculated by segmenting the liver in the CT. Segmentations were made by an independent person blind to those used during the registration process in order to guarantee the independence of the simulation step with respect to the registrations.

To simulate the partial volume effect in MRI (Tohka et al., 2004), a 3D low-pass Gaussian filter with a standard deviation for the Gaussian kernel of [1,1,3] was applied after the intensity transformation.

Gd–EOB–DTPA-enhanced MRI images commonly show better edge enhancement than CT images. To simulate this particular feature, borders were first calculated by morphological edge detection and added by summation to the existing image.

The MRI signal is corrupted by an additive noise process (Kwan et al., 1999). As noise distributions in MRI images are nearly white Gaussian for signal-to-noise ratios (SNR) greater than 2 (Gudbjartsson and Patz, 1995), we added independent realizations of white Gaussian noise to our simulated dataset. We measured the amount of added noise as a signal-to-noise ratio according to Bushberg et al. (2002):

$$\mathrm{SNR} = A/\sigma_n \tag{20}$$

where A is the mean image pixel intensity, and σ_n is the standard deviation of the Gaussian noise. Different levels of Gaussian noise were added to the simulated data ranging from SNR 3 to SNR 7.

Additionally, known transformations were applied to the original CT images to generate reference images for the registration experiments. The transformations were modeled using a closed-form function that defines the spatial dependence of the deformation, mimicking nonrigid organ movements due to respiration and volume changes along time caused by differences in patient weight, organ disposition, or liver volume growth due to illness evolution or portal vein embolization. In our transformation model we assume that the deformation is 0 in the center of the body and maximum at a liver distance, as the soft-tissue motion of the liver is highly influenced by the motion of both the diaphragm and the ribcage (Villard et al., 2011). According to some sources, local liver

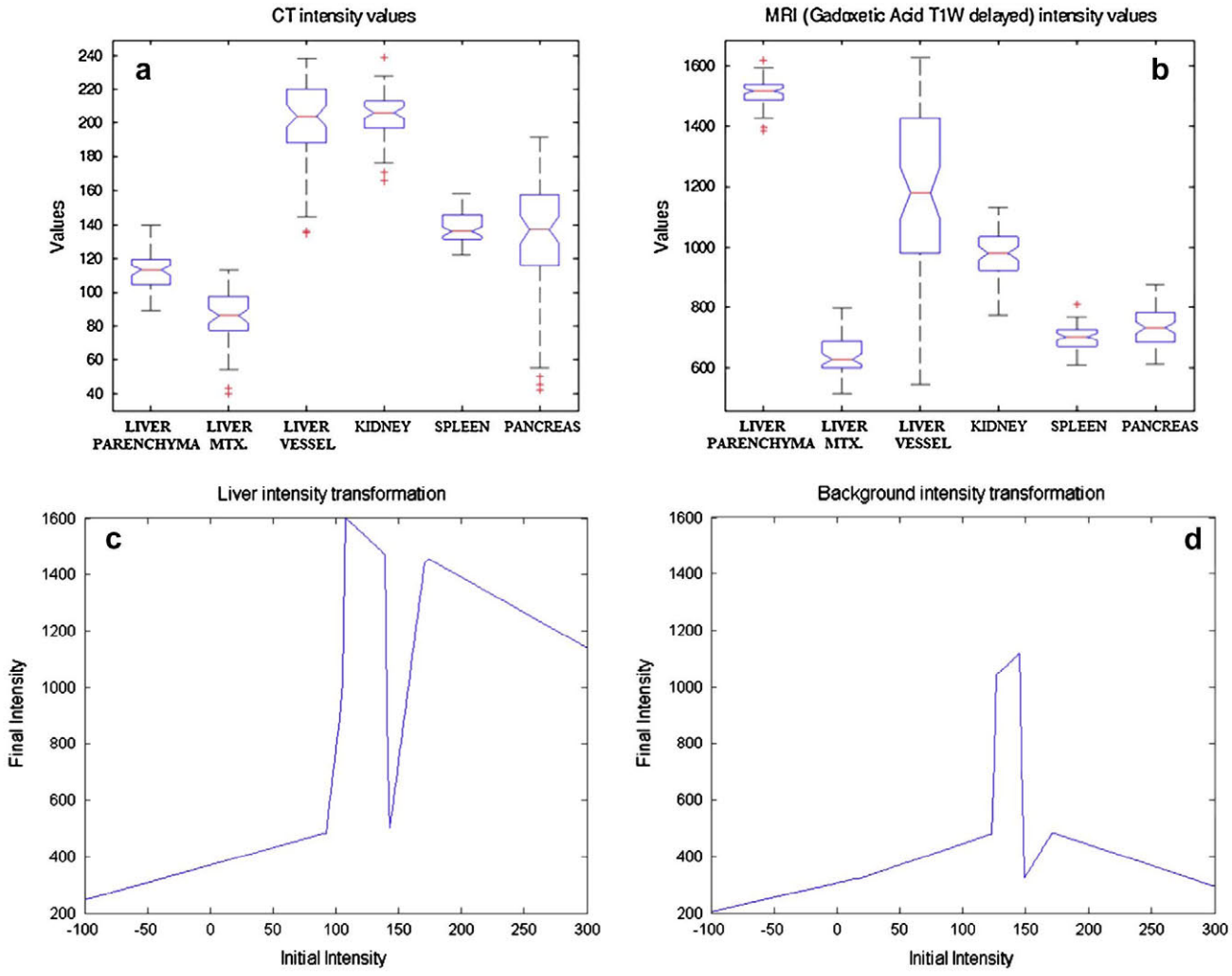

Fig. 3. Intensity distribution analysis in contrast-enhanced portal-phase CT (a) and delayed T1-weighted Gd–EOB–DTPA-enhanced MRI (b) for abdominal organs and important regions inside the liver (parenchyma, metastasis and vessels). Nonlinear intensity transformations applied in liver region (c) and liver background (d) to generate MRI simulated images from CT images.

deformation due to respiration can range from 10 to 26 mm in amplitude between the extremes of the respiratory cycle (Blackall et al., 2005; Clifford et al., 2002; Rohlfing et al., 2001). Moreover, we approximate the deformation as a continuous movement. Therefore, we represent the dependency of the deformation on the distance to the center of the image by using a sinusoidal function that allows us to have a symmetric deformation all around the contour of the body with maximum value in the center of the liver. The simulated deformation is defined by $\mathbf{t}(\mathbf{i}) = \{t_k(i_k)\}_{k=1,\,2,\,3}$, where $\mathbf{i} \in I \subset \mathbb{Z}^3$ and I is the 3-dimensional discrete interval representing the set of all voxel coordinates in the image. $\mathbf{t}(\mathbf{i})$ is applied voxel by voxel as defined by the equation:

$$t_k(i_k) = i_k - m_k \cdot \sin\left(\frac{x_{c,k} - i_k}{|x_{c,k} - x_{w,k}|} \cdot \frac{\pi}{2}\right) \tag{21}$$

where $\mathbf{x_c}$ are the voxel coordinates with minimum deformation, $\mathbf{x_w}$ are the voxel coordinates with maximum deformation and $\mathbf{m}$ is the maximum deformation. $\mathbf{x_c}$ represents the center of the image and $\mathbf{x_w}$ represents the points at 1/3 of the extreme of the image that comprise the liver in all the models. Therefore, these parameters depend on the image size $\mathbf{s_{im}} = \{s_{\mathrm{im},k}\}_{k=1,\,2,\,3}$ as follows:

$$\begin{aligned} \mathbf{x_c} &= p_c \cdot \mathbf{s_{im}} \\ \mathbf{x_w} &= p_w \cdot \mathbf{s_{im}} \end{aligned} \tag{22}$$

where $p_c = 0.5$ and $p_w = 1/3$. Considering the literature references about local liver deformation (Blackall et al., 2005; Clifford et al., 2002; Rohlfing et al., 2001), we decided to apply to each of our 63 models a maximum deformation value that varies randomly between 4 mm and 28 mm at liver level. m_k represents the magnitude of the maximum deformation for each dimension and takes random values in the range [4,28] (mm).

An example of a synthetic delayed T1-weighted Gd–EOB–DTPA-enhanced MRI can be seen and compared with a real MRI image in Fig. 4 as well as an example of a simulated deformation.

3.1.2. Real images dataset

A dataset consisting of seven clinical subjects with a wide variety of pathological scenarios was used. Each case has one contrast-enhanced portal-phase CT and one delayed T1-weighted Gd–EOB–DTPA-enhanced MRI from a retrospective clinical dataset. The contrast-enhanced portal-phase helical CTs were performed with a 16-MDCT scanner (Brilliance 16; Philips Medical Systems, Eindhoven, The Netherlands) in all cases. The scanning parameters were 120 kVp, 250–300 mA s, 2-mm slice thickness with an overlap of 1 mm (pitch, 0.9), and a single-breath-hold helical acquisition. The images were obtained in the craniocaudal direction. Hepatic portal-phase scanning began 70 s after injection of 120 ml of a nonionic iodinated contrast agent (Ioversol, Optiray Ultraject 300; Covidien). For delayed T1-weighted Gd–EOB–DTPA-enhanced MRI, 20-min delayed hepatobiliary phase images were obtained with a T1-weighted 3D turbo-field-echo sequence (T1 high-resolution isotropic volume examination, THRIVE; Philips Medical Systems, Eindhoven, The Netherlands) (3.4/1.8; flip angle 10°; matrix size, 336 × 206; bandwidth, 995.7 Hz/pixel) with a 2-mm section thickness, no intersection gap, and a field of view of 32–38 cm. Details regarding clinical information are summarized in Table 1.

MRI images were manually aligned onto the corresponding CT by a point-based rigid registration.

The images were then cropped in axes X, Y, and Z to restrict the subsequent image-processing steps to the complete body region at liver level. The images were then resampled to pixel size [1,1,1] mm, guaranteeing isotropy. CT was used as the reference image, and MRI as the test image.

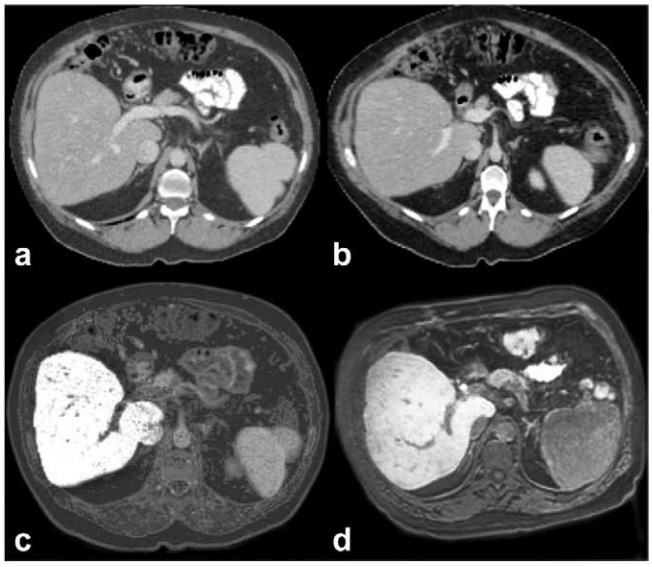

Fig. 4. (a) Original CT, (b) CT with simulated deformation, (c) synthetic gadoxetic acid MRI, (d) real gadoxetic acid MRI.

3.2. Error measures

3.2.1. Measures on the simulated dataset

Registration of simulated CT and MRI datasets was evaluated in terms of geometric error by comparing the resulting transformation with the applied analytical one on a voxel-by-voxel basis using the warping index (WI) (Thévenaz et al., 1998). The WI calculation was restricted to the liver region:

$$\mathrm{WI} = \frac{1}{|R|}\sum_{\mathbf{i}\in R}\|\mathbf{g}(\mathbf{i}) - \mathbf{g}^*(\mathbf{i})\| \tag{23}$$

where $\mathbf{g}^*$ is the true deformation, R represents the set of all voxel coordinates inside the liver, and $\|\cdot\|$ the Euclidean distance.

3.2.2. Measures on the real dataset

To establish an independent validation procedure, radiologists annotated all real images manually, defining a set of 10 intrinsic anatomical hepatic landmarks for each pair of images. Registration results were evaluated in terms of the mean distance error between corresponding anatomical landmarks before and after registration for each subject (landmark-based mean errors). Landmarks were located in vessel intersections, hepatic fissures and ligaments, and small lesions.

Because of the high dependency of error results on the accuracy of the landmark selections, additional error criteria were also considered. For this purpose, the liver was manually segmented in the CT and MRI images. Segmentations were made by an independent expert blind to those used during the registration process in order to guarantee the independence of the registrations with respect to the validation. Comparing liver segmentation before and after registration allows calculation of surface-based mean errors (ME):

$$\mathrm{ME} = \frac{1}{|S|}\sum_{\mathbf{i}\in S} d_{\mathbf{i}} \tag{24}$$

where S is an N-dimensional discrete interval representing the set of all voxel coordinates in both liver segmentation surfaces; it is obtained by considering voxels inside the segmented liver with at least one of their 18 nearest neighbors not belonging to the liver. $d_{\mathbf{i}}$ represents the Euclidean distance of a voxel $\mathbf{i}$ to the closest one in the other segmentation. ME (mm) is zero for two perfectly registered surfaces.

Table 1
Real dataset clinical description (*Roman numerals represent Couinaud hepatic segments (Couinaud, 1999)).

Subject	Clinical information	Image dates	CT-visible lesions	MRI-visible lesions
1	Hepatectomy Metastases Chemotherapy	MRI 26 days post-CT	1 in hepatic duct	1 in hepatic duct 1 in IVb*
2	Metastases Chemotherapy	CT 45 days post-MRI	0	1 in II/III 1 in IVa/VIII 1 in VI 1 in I
3	Metastases	MRI 21 days post-CT	1 in IV 1 in VIII	1 in VIII
4	Hepatectomy Metastases	MRI 10 months post-CT	0	0
5	Metastases Cholecystectomy	MRI 12 days post-CT	3 in VIII 1 in IV 1 in II	1 in VIII 1 in VII/VIII 1 in II
6	Metastases Sectorectomy	MRI 4 months post-CT	0	0
7	Metastases	MRI 1 month post-CT	1 in VII	1 in IV 1 in II

3.3. Parameter optimizations

To investigate the best parameter combination, we tested the performance of the algorithm with one real training subject. Common parameters in the intensity-based nonrigid registration algorithm are:

- degrees of the B-spline functions: m, n, m_1, and m_2,
- knot spacing of the transformation grid: $\mathbf{h}$,
- weight for the regularization term: γ,
- number of bins for the intensity probability distributions: n_{binsT}, n_{binsR},
- number of multiresolution levels: after some initial experiments, this was fixed at 3.

3.3.1. Choosing the B-spline degrees

The B-spline degrees for the image, m, and deformation model, n, were chosen as cubic because previous studies have shown that these perform better than linear and quadratic splines (Kybic and Unser, 2003). However, for the B-spline joint probability distribution model (m_1, m_2), the chosen degree was quadratic. By using quadratic B-splines, we ensure derivability of the joint probability distributions and avoid an increase in histogram dispersion.

3.3.2. Choosing the node spacing and the regularization weight

The main criterion for choosing the knot spacing $\mathbf{h}$ in (5) and the regularization weight γ in (6) is the estimated intrinsic resolution (smoothness) of the deformation to be recovered. To estimate these optimum parameters, multiple registrations were run using MI and OF-MI with different values for the node spacings in the three dimensions $h_k \in \{12,14,16,18,20\}$, $(k = 1,2,3)$ given in mm and the weight $\gamma \in \{0, 0.001, 0.002, \ldots, 0.01\}$ for the regularization term. Surface-based ME values after applying registrations based on OF-MI and MI are shown in Figs. 5 and 6. The optimum parameters are $h_k = 18$ mm $\forall k$ and $\gamma = 0.001$ for both MI and OF-MI.

3.3.3. Choosing the number of bins in the histogram

A low number of bins reduces the noise level in MI and helps avoid trapping the optimization in a local minimum (Kim et al., 1997) while increasing the approximation error (Thévenaz and Unser, 1996). In this work we fixed the number of bins to 32×32 for all resolution levels.

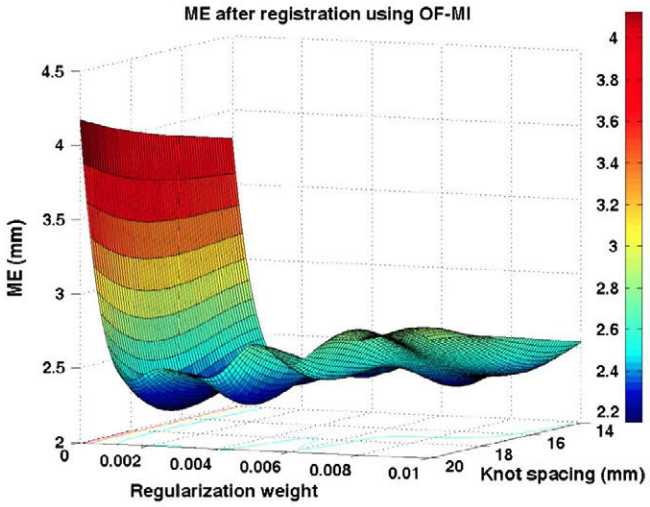

Fig. 5. Surface-based ME values after applying registrations based on OF-MI for different knot spacings h_k $\forall k$ and regularization weights γ in the real training subject.

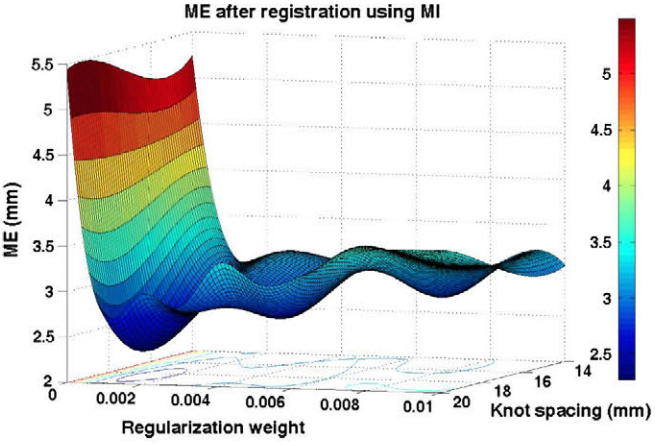

Fig. 6. Surface-based ME values after applying registrations based on MI for different knot spacings h_k $\forall k$ and regularization weight γ in the real training subject.

3.4. Results

3.4.1. Results with simulated dataset

Warping index (WI) results for the 63-subject dataset are shown in Table 2. First, we can observe an important improvement for the nonrigid registrations compared with the initial values for both MI and OF-MI criteria.

Based on the Kolmogorov–Smirnov test, we cannot assume normality for the pair-wise difference of the WI values distribution. Therefore, we apply the Wilcoxon matched-pairs signed-rank test to study the significant difference of the registration error measures. A significant reduction in WI values using registrations based on OF-MI compared with those based on MI ($p < 0.01$) was confirmed.

Both methods are affected by noise, but OF-MI presents a more robust behavior with respect to SNR changes (Fig. 7).

3.4.2. Results with real dataset

Visual inspection of the results shows important qualitative improvements after applying nonrigid registration to the images, especially when using OF-MI. Specific structures inside the liver are registered better when using OF-MI, which facilitates accurate localization of lesions from the MRI into the CT for surgery planning. Fig. 9 shows the fusion of CT and MRI before and after registration with MI and OF-MI for one of the subjects. Even when most of the organ surfaces are visually well registered with both criteria; the registration with OF-MI is better in some critical areas affecting the inner liver vessels (see Figs. 8 and 10). Fig. 9 shows hepatic surfaces registration improvements with OF-MI with respect to the initial scenario and with respect to the use of MI in the nonrigid registration. In Fig. 10 a detailed view of the fitting of a subset of the vascular branches is given. As can be seen from Fig. 10(b and e) versus (c and f) in comparison to the use of MI, the use of OF-MI results in a considerable better alignment between these vessels.

Table 2
Warping Index results with simulated dataset ($\gamma = 0.001$ and $h_k = 18$ mm $\forall k$).

	Before registration	After registration MI	After registration OF-MI
WI (mm)			
Mean	11.39	4.77	4.28
Std. dev.	2.56	2.63	2.51
Median	11.124	3.87	3.33
Min.	5.38	1.84	1.32
Max.	16.39	14.18	13.18

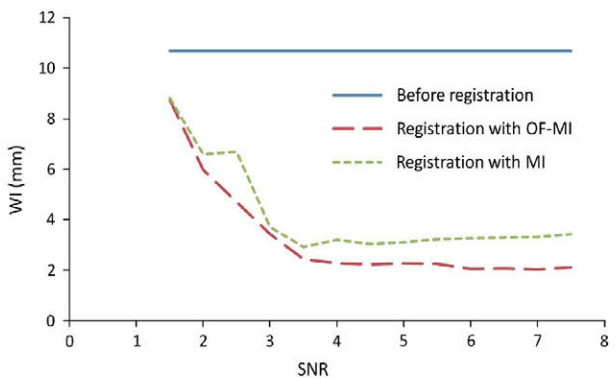

Fig. 7. Warping Index results after applying registrations with MI and OF-MI to a simulated dataset with SNR ranging from 1 to 8 (registration parameters: $\gamma = 0.001$ and $h_k = 18$ mm $\forall k$.

Numerical registration results are summarized in Table 3. Better results are obtained with respect to all criteria with OF-MI than with MI, with maximum improvements of 1.27 mm for the landmark-based mean geometric errors (subject 5) and 2.39 mm for the surface-based mean errors (subject 5).

In order to see the effect on the registration results of segmentation accuracy when calculating the masks for the OFMI criteria, we have performed independent registration experiments on all seven data sets checking the effect of inter-subject segmentation errors within the real context. Therefore, when using masks for the OFMI criteria segmented by an additional non-expert user, we observed a landmark-based mean error of 7.42 mm, on average for all seven data sets, also smaller than that obtained using MI (7.55 mm). As the inter-subject variability of the segmentation accuracy using the semi-automatic method described in Fernandez-de-Manuel et al. (2009) and Jimenez-Carretero et al. (2011) is 1.35 mm on average, we can conclude that for segmentation errors due to inter-subject variability and smaller than 1.35 mm, the OFMI registration method gives consistent and robust results, better to those obtained with standard MI.

Additionally, Fig. 11 shows the effect on the registration results of artificial segmentation errors in the mask for the OFMI criteria. We have applied morphological dilation and erosion on the initial segmentation of one real subject using a sphere of different radius from 1 to 4 voxels as structuring element, and we have studied the effect on the final results. Assuming that a segmentation obtained by applying the semi-automatic method described in Fernandez-de-Manuel et al. (2009) and Jimenez-Carretero et al. (2011) is the proper one, we express the errors using the surface-based mean errors (ME) (mm) (24) between the original segmentation and the dilated/eroded versions. We can see that with mean errors in the masks used in the OFMI criteria smaller than 3 mm, the final registration results are always better than those of the standard MI. Additionally, we have found that the OF-MI metric is less sensitive to errors resulting from erosions than from dilations of the initial mask.

4. Discussion

We have described a nonrigid registration framework that takes advantage of available expert liver segmentations in clinical protocols to ensure good alignment of the inner structures of the liver. The validation of the proposed registration method shows that the OF-MI metric improves the results obtained with the classical formulation of MI. Maximum improvements were as high as 1.27 mm for the mean landmark-based geometric errors (subject 5) reaching up to 6 mm for some particular landmarks. The comparison of Fig. 10(b and e) versus Fig. 10(c and f) illustrates the contribution of OF-MI, that provides a substantially better alignment of vessels. The significance of these improvements should be considered in the context of the target application: liver surgery planning. In this scenario, the definition of the surgical approach may depend on the accuracy of the registration in certain areas inside the liver and therefore any improvement in the registration results affecting those areas will facilitate these decisions. Even when most of the organ surface is visually well registered with MI or OF-MI, and the numerical difference between the methods is not large; the registration with OF-MI becomes significant in some critical areas affecting the liver parenchyma and inner vascular structure.

There are a number of translational examples in liver surgery planning where differences of a few millimeters in the spatial precision when identifying the lesions and vessel irrigations may materialize into success (eradication) or failure (persistence) of the treatment of the underlying cancer. For instance, during the

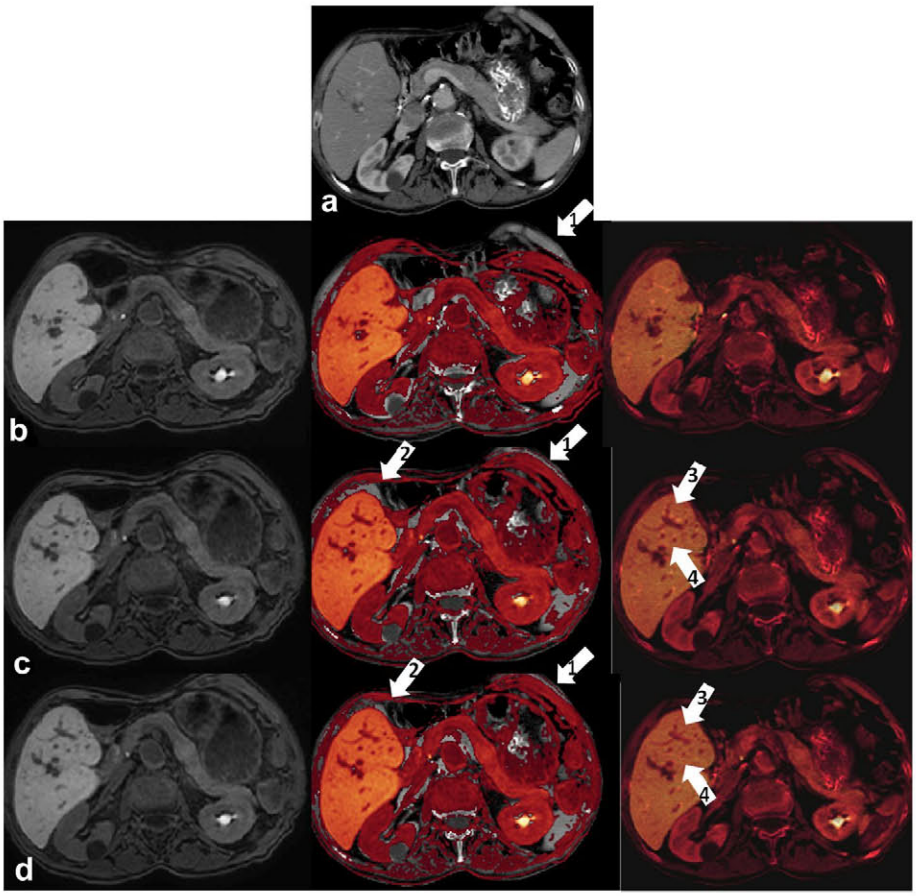

Fig. 8. (a) Contrast-enhanced portal-phase CT subject 1 (fixed image); (b) Gd–EOB–DTPA-enhanced MRI before registration (first column) and fusion with CT (overlay fusion – second column – and multiplication fusion – third column); (c) Gd–EOB–DTPA-enhanced MRI after registration with MI (first column) and fusion with CT (overlay fusion – second column – and multiplication fusion – third column); (d) Gd–EOB–DTPA-enhanced MRI after registration with OF-MI (first column) and fusion with CT (overlay fusion – second column and multiplication fusion – third column). Arrows number 1 show improvements in body contour fitting after registration. Arrows number 2 show that the fitting of liver boundaries is performed better when using OF-MI. Arrows number 3 and 4 show that the fitting of several liver vessels is performed better when using OF-MI.

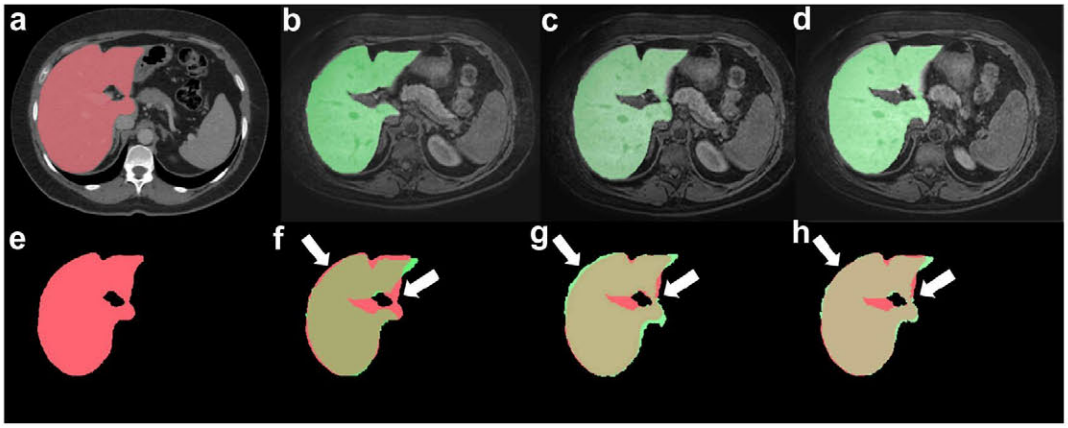

Fig. 9. CT liver segmentation in red (a, e, f, g, h) and MRI liver segmentation in green: before registration (b and f), after registration with MI (c and g) and after registration with OF-MI (d and h) in subject 7. Comparison of liver segmentation before and after registration (f, g, h). Note the better alignment of the liver boundaries when using OF-MI (h) as compared to the classical formulation of MI (g) (see white arrows). (For interpretation of the references to color in this figure legend, the reader is referred to the web version of this article.)

ablation of focal liver tumors assisted by the fusion of preoperative CT/MRI and intraoperative ultrasound (Jung et al., 2012), the target selection and calculation of the lesioń s ablative volume from the pre-procedure images must accurately be blended with the real-time ultrasound in order to place the thermal electrode on the selected targets. Millimetric displacement and tracking inaccuracy due to minor errors in the registration step may cause treatment failure (Krücker et al., 2011). The accuracy in the preoperative step registering the CT and the MRI becomes as important as the intra-operative step. Another illustrative example is the surgery planning of patients with preoperative hepatic dysfunction (cirrhosis or post-chemotherapy liver toxicity) (Dokmak et al., 2012),

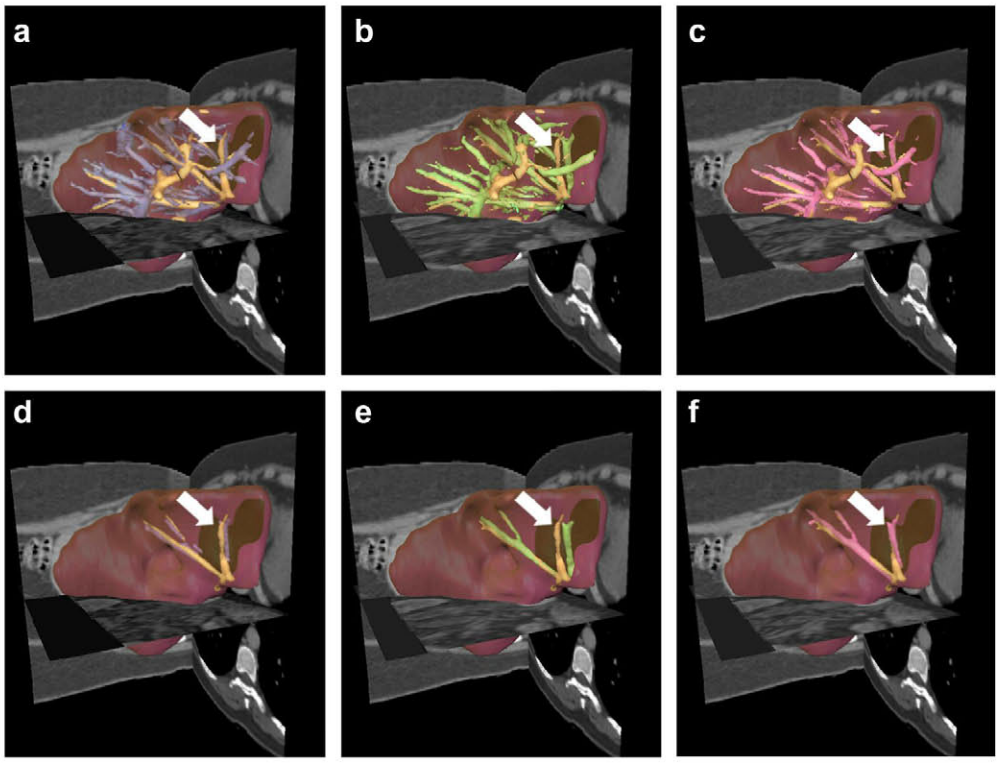

Fig. 10. Contrast-enhanced portal-phase CT of subject 7 (sagittal and transversal plains), Gd–EOB–DTPA-enhanced MRI (coronal plain), CT liver segmentation (red structure), and vessel segmentations from the CT (orange), as well as from the MRI (purple, green, pink), before registration (a and d), after registration optimizing classical MI (b and e), and after registration by optimizing OF-MI (c and f). Upper row: complete vascular branchs, lower row: detail of one particular vascular branch. Note the better alignment of the vascular branches when optimizing OF-MI (c and f) as compared with MI (b and e) (see white arrows). (For interpretation of the references to color in this figure legend, the reader is referred to the web version of this article.)

Table 3
Results with real dataset. ($\gamma = 0.001$ and $h_k = 18$ mm $\forall k$).

	Before registration	After registration MI	After registration OF-MI
Landmark-based error (mm)			
Mean	9.61	7.55	7.07
Std. dev.	1.83	2.09	1.88
Median	10.04	8.07	6.86
Min.	7.08	3.74	3.62
Max.	12.08	10.04	8.91
Surface-based mean error (mm)			
Mean	4.79	3.68	3.20
Std. dev.	0.89	1.00	0.52
Median	5.06	3.79	3.23
Min.	3.14	2.42	2.46
Max.	5.74	5.62	3.93

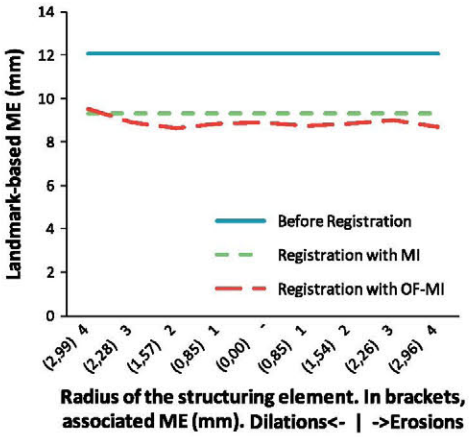

Fig. 11. Landmark-based mean error before and after registration using MI and OF-MI for a real subject. Effect in the OF-MI results of realistic amounts of segmentation errors when calculating the masks for the OFMI criteria (ME with respect to the proper segmentation in brackets).

multiple lesions (Gold et al., 2008), or undergoing repeated liver resections. In these patients, major hepatic surgery with ample oncological margins larger than 10 mm cannot be performed and the safest approach is a parenchymal-sparing liver resection that requires a precise study of the oncological margin of each lesion and lesion-to-vascular topography. In (Casciola et al., 2011), the authors point out the necessity of using both a contrast enhanced CT and a liver gadoxetic acid-enhanced MRI for robot-assisted parenchymal-sparing liver surgery in order to evaluate, during the preoperative work-up, the technical feasibility of a liver resection and the viability of a minimally invasive approach. Different cases where the tumor was in contact with a main portal branch or with a hepatic vein were studied in Casciola et al. (2011), describing the different surgery strategies depending on the level of contact between the lesion and the vessel. The proper identification and fitting of the vessels among imaging modalities facilitates the accurate delimitation of the adjacency of tumors and veins and the proper detection of vascular invasion determining whether the patient is unresectable or eligible for surgery.

One possible limitation of the OF-MI is the influence of liver segmentation errors in the registration accuracy. The experiments show that for mean errors of 1.35 mm due to inter-subject variability in the liver segmentation masks, the final registration results still improved those obtained using standard MI. Therefore, errors in the liver segmentations defined in the clinical protocol hardly

modify the results, making the applicability of the proposed method in clinical environment more realistic and reliable.

Finally, this work can also be useful in other therapeutic applications. Scenarios such as radiotherapy treatment planning using multimodal imaging (Kessler et al., 1991; Tan et al., 2010; Thorwarth et al., 2013) could also benefit from the advantages of the inclusion of additional regional information using OF-MI. Considering that segmentations are normally available for the dosimetry planning (Acosta et al., 2010; Bazalova and Graves, 2011; Lu et al., 2011), their use for the registration could imply benefits without affecting the clinical protocols.

5. Conclusions

In this work we have proposed a multimodal nonrigid registration framework to characterize liver lesions using simultaneously contrast-enhanced portal-phase CT and delayed T1-weighted Gd–EOB–DTPA-enhanced MRI using OF-MI, and we have compared it with the classical formulation of MI. We took advantage of actual liver segmentation available in standard clinical protocols and we used them in the criterion. This solution allows the statistical dependence between the two modalities to differ inside and outside the organ of interest.

We have shown important improvements in all considered validation criteria after applying nonrigid registration to simulated and real multimodal liver studies, in comparison with unaligned images. The improvement was in general better when using OF-MI than with MI. We tested and confirmed the statistical significance of the improvement in the simulated data ($p < 0.01$). Specific structures inside the liver are registered better when using OF-MI, facilitating more accurate localization of lesions from the MRI into the CT for surgery planning. In addition, OF-MI presents more robust behavior with respect to SNR changes and more stable results with smaller dispersion than MI.

Acknowledgments

This work was supported in part by Spain's Ministry of Science and Innovation through the Project TEC2010-21619-C04-03/01, CDTI–CENIT (AMIT), INNPACTO (PRECISION & XIORT) IPT-300000-2010-3, Instituto de Salud Carlos III (PI09/91058, PI09/91065, PI09/90568 and PI09/90987), Comunidad de Madrid (ARTEMIS S2009/DPI-1802) and the European Regional Development Funds (FEDER). Jan Kybic was supported by Czech Science Foundation project P202/11/0111.

Appendix A

A.1. Derivatives of OF-MI

The partial derivatives of the $E_{\text{OF-MI}}$ with respect to $\mathbf{c_j}$ (17) are:

$$\frac{\partial(E_{\text{OF-MI}})}{\partial c_{\mathbf{j},k}} = \sum_{\mathbf{i}\in I_a} \frac{\partial(E_{\text{OF-MI}})}{\partial f_w(\mathbf{i})} \cdot \frac{\partial f_t^c(\mathbf{x})}{\partial x_k}\bigg|_{\mathbf{x}=\mathbf{g}(\mathbf{i})} \cdot \frac{\partial g_k(\mathbf{i})}{\partial c_{\mathbf{j},k}} \tag{A.1}$$

where

$$\frac{\partial(E_{\text{OF-MI}})}{\partial f_w(\mathbf{i})} = -\sum_{\forall t}\sum_{\forall r}\sum_{\forall l} \frac{\partial p(t,r,l;\mathbf{c})}{\partial f_w(\mathbf{i})} \cdot \log\frac{p(t,r,l;\mathbf{c})}{p_T(t;\mathbf{c})} \tag{A.2}$$

Differentiating the joint probability distribution $p(t,r,l;\mathbf{c})$ with respect to the warped image at $\mathbf{i}$ in (A.2) can be expressed as:

$$\frac{\partial p(t,r,l;\mathbf{c})}{\partial f_w(\mathbf{i})} = -\frac{1}{|I_c|}\cdot\frac{nbinsT-1}{f_{w\max}-f_{w\min}} \cdot P_{\Omega_i}(\mathbf{i}) \cdot \beta_{m_2}(r-\rho(\mathbf{i};\mathbf{c})) \cdot \frac{\partial \beta_{m_1}(\xi)}{\partial \xi}\bigg|_{\xi=t-\tau(\mathbf{i};\mathbf{c})} \tag{A.3}$$

The explicit expression for the derivative of the B-spline function is:

$$\frac{\partial \beta_{m_1}(\xi)}{\partial \xi} = \beta_{m_{1-1}}(\xi+1/2) - \beta_{m_{1-1}}(\xi-1/2) \tag{A.4}$$

The partial derivatives of f_t^c (4) are calculated as a tensor product (Kybic, 2001):

$$\frac{\partial f_t^c}{\partial x_k} = \sum_{\mathbf{i}\in I_a} a_{\mathbf{i}} \frac{\partial \beta_m(x_k)}{\partial x_k} \prod_{\substack{\lambda=1 \\ \lambda\neq k}}^{N} \beta_m((g_\lambda(x_\lambda))) \tag{A.5}$$

Finally, the derivative of the deformation function is calculated from (5):

$$\frac{\partial g_k(\mathbf{i})}{\partial c_{\mathbf{j},k}} = \beta_n(\mathbf{i}/\mathbf{h}-\mathbf{j}) \tag{A.6}$$

where k is the dimension of the N-dimensional $\mathbf{c_j}$ deformation parameters.

References

Acosta, O., Dowling, J., Cazoulat, G., Simon, A., Salvado, O., De Crevoisier, R., Haigron, P., 2010. Atlas based segmentation and mapping of organs at risk from planning ct for the development of voxel-wise predictive models of toxicity in prostate radiotherapy, prostate cancer imaging. In: Computer-Aided Diagnosis, Prognosis, and Intervention. Springer, pp. 42–51.

Archip, N., Tatli, S., Morrison, P., Jolesz, F., Warfield, S.K., Silverman, S., 2007. Non-rigid registration of pre-procedural MR images with intra-procedural unenhanced CT images for improved targeting of tumors during liver radiofrequency ablations. Medical Image Computing and Computer-Assisted Intervention-MICCAI, pp. 969–977.

Bazalova, M., Graves, E.E., 2011. The importance of tissue segmentation for dose calculations for kilovoltage radiation therapy. Medical Physics 38, 3039.

Blackall, J.M., Penney, G.P., King, A.P., Hawkes, D.J., 2005. Alignment of sparse freehand 3-D ultrasound with preoperative images of the liver using models of respiratory motion and deformation. IEEE Transactions on Medical Imaging 24, 1405–1416.

Bluemke, D.A., Paulson, E.K., Choti, M.A., DeSena, S., Clavien, P.A., 2000. Detection of hepatic lesions in candidates for surgery: comparison of ferumoxides-enhanced MR imaging and dual-phase helical CT. American Journal of Roentgenology 175, 1653–1658.

Bushberg, J.T., Bushberg, J.T., Seibert Jr., J.A., E.M.I., Boone, J.M., 2002. The Essential Physics of Medical Imaging. Williams & Wilkins.

Carrillo, A., Duerk, J.L., Lewin, J.S., Wilson, D.L., 2000. Semiautomatic 3-D image registration as applied to interventional MRI liver cancer treatment. IEEE Transactions on Medical Imaging 19, 175–185.

Casciola, L., Patriti, A., Ceccarelli, G., Bartoli, A., Ceribelli, C., Spaziani, A., 2011. Robot-assisted parenchymal-sparing liver surgery including lesions located in the posterosuperior segments. Surgical Endoscopy 25, 3815–3824.

Clifford, M.A., Banovac, F., Levy, E., Cleary, K., 2002. Assessment of hepatic motion secondary to respiration for computer assisted interventions. Computer Aided Surgery 7, 291–299.

Couinaud, C., 1999. Liver anatomy: portal (and suprahepatic) or biliary segmentation. Digestive Surgery 16, 459–467.

Crum, W.R., Hartkens, T., Hill, D., 2004. Non-rigid image registration: theory and practice. British Journal of Radiology 77, S140.

Dokmak, S., Agostini, J., Jacquin, A., Cauchy, F., Farges, O., Belghiti, J., 2012. High risk of biliary fistula after isolated segment VIII liver resection. World Journal of Surgery 36, 2692–2698.

Donati, O.F., Hany, T.F., Reiner, C.S., von Schulthess, G.K., Marincek, B., Seifert, B., Weishaupt, D., 2010. Value of retrospective fusion of PET and MR images in detection of hepatic metastases: comparison with 18F-FDG PET/CT and Gd–EOB–DTPA-enhanced MRI. Journal of Nuclear Medicine 51, 692–699.

Fernandez-de-Manuel, L., Rubio, J.L., Ledesma-Carbayo, M.J., Pascau, J., Tellado, J.M., Ramón, E., Desco, M., Santos, A., 2009. 3D Liver Segmentation in Preoperative CT Images using a Level-Sets Active Surface Method, Annual International Conference of the IEEE Engineering in Medicine and Biology Society. EMBS, Minneapolis, pp. 3625–3628.

Fernandez-de-Manuel, L., Ledesma-Carbayo, M.J., Jimenez-Carretero, D., Pascau, J., Rubio-Guivernau, J.L., Tellado, J.M., Ramon, E., Desco, M., Santos, A., 2011. Liver Segmentation and Volume Estimation from Preoperative CT Images in Hepatic Surgical Planning: Application of a Semiautomatic Method Based on 3D Level Sets. Theory and Applications of CT Images. InTech, pp. 79–94.

Gold, J.S., Are, C., Kornprat, P., Jarnagin, W.R., Gönen, M., Fong, Y., DeMatteo, R.P., Blumgart, L.H., D'Angelica, M., 2008. Increased use of parenchymal-sparing surgery for bilateral liver metastases from colorectal cancer is associated with improved mortality without change in oncologic outcome: trends in treatment over time in 440 patients. Annals of Surgery 247, 109–117.

Gudbjartsson, H., Patz, S., 1995. The Rician distribution of noisy MRI data. Magnetic Resonance in Medicine 34, 910–914.

Hammerstingl, R., Huppertz, A., Breuer, J., Balzer, T., Blakeborough, A., Carter, R., Fuste, L.C., Heinz-Peer, G., Judmaier, W., Laniado, M., 2008. Diagnostic efficacy of gadoxetic acid (Primovist)-enhanced MRI and spiral CT for a therapeutic strategy: comparison with intraoperative and histopathologic findings in focal liver lesions. European Radiology 18, 457–467.

Handels, H., Ehrhardt, J., 2009. Medical image computing for computer-supported diagnostics and therapy advances and perspectives. Methods of Information in Medicine 48, 11–17.

Heimann, T., van Ginneken, B., Styner, M.A., Arzhaeva, Y., Aurich, V., Bauer, C., Beck, A., Becker, C., Beichel, R., Bekes, G., Bello, F., Binnig, G., Bischof, H., Bornik, A., Cashman, P.M.M., Chi, Y., Cordova, A., Dawant, B.M., Fidrich, M., Furst, J.D., Furukawa, D., Grenacher, L., Hornegger, J., Kainmuller, D., Kitney, R.I., Kobatake, H., Lamecker, H., Lange, T., Lee, J., Lennon, B., Li, R., Li, S., Meinzer, H.P., Nemeth, G., Raicu, D.S., Rau, A.M., van Rikxoort, E.M., Rousson, M., Rusko, L., Saddi, K.A., Schmidt, G., Seghers, D., Shimizu, A., Slagmolen, P., Sorantin, E., Soza, G., Susomboon, R., Waite, J.M., Wimmer, A., Wolf, I., 2009. Comparison and evaluation of methods for liver segmentation from CT datasets. IEEE Transactions on Medical Imaging 28, 1251–1265.

Heinrich, M., Jenkinson, M., Brady, M., Schnabel, J., 2012a. Textural mutual information based on cluster trees for multimodal deformable registration. IEEE International Symposium on Biomedical Imaging, ISBI. IEEE, Barcelona, pp. 1471–1474.

Heinrich, M.P., Jenkinson, M., Bhushan, M., Matin, T., Gleeson, F.V., Brady, S.M., Schnabel, J.A., 2012b. MIND: modality independent neighbourhood descriptor for multi-modal deformable registration. Medical Image Analysis 16, 1423–1435.

Hermosillo, G., Chefd'Hotel, C., Faugeras, O.D., 2002. Variational methods for multimodal image matching. International Journal of Computer Vision 50, 329–343.

Hill, D.L.G., Batchelor, P.G., Holden, M., Hawkes, D.J., 2001. Medical image registration. Physics in Medicine and Biology 46, R1–R45.

Jimenez-Carretero, D., Fernandez-de-Manuel, L., Pascau, J., Tellado, J.M., Ramon, E., Desco, M., Santos, A., Ledesma-Carbayo, M.J., 2011. Optimal multiresolution 3D level-set method for liver segmentation incorporating local curvature constraints. In: Annual International Conference of the IEEE Engineering in Medicine and Biology Society, EMBS, Boston, Massachusetts, USA, pp. 3419–3422.

Jung, E.M., Friedrich, C., Hoffstetter, P., Dendl, L.M., Klebl, F., Agha, A., Wiggermann, P., Stroszcynski, C., Schreyer, A.G., 2012. Volume navigation with contrast enhanced ultrasound and image fusion for percutaneous interventions: first results. PLoS One 7, e33956.

Kessler, M.L., Pitluck, S., Petti, P., Castro, J.R., 1991. Integration of multimodality imaging data for radiotherapy treatment planning. International Journal of Radiation Oncology* Biology* Physics 21, 1653–1667.

Kim, B., Boes, J.L., Frey, K.A., Meyer, C.R., 1997. Mutual information for automated unwarping of rat brain autoradiographs. NeuroImage 5, 31–40.

Kong, G., Jackson, C., Koh, D., Lewington, V., Sharma, B., Brown, G., Cunningham, D., Cook, G.J.R., 2008. The use of 18F-FDG PET/CT in colorectal liver metastases—comparison with CT and liver MRI. European Journal of Nuclear Medicine and Molecular Imaging 35, 1323–1329.

Krücker, J., Xu, S., Venkatesan, A., Locklin, J.K., Amalou, H., Glossop, N., Wood, B.J., 2011. Clinical utility of real-time fusion guidance for biopsy and ablation. Journal of Vascular and Interventional Radiology 22, 515–524.

Kwan, R.K.S., Evans, A.C., Pike, G.B., 1999. MRI simulation-based evaluation of image-processing and classification methods. IEEE Transactions on Medical Imaging 18, 1085–1097.

Kybic, J., 2001. Elastic Image Registration using Parametric Deformation Models. Ecole Polytechnique Federale de Lausanne, Lausanne.

Kybic, J., Unser, M., 2003. Fast parametric elastic image registration. IEEE Transactions on Image Processing 12, 1427–1442.

Kybic, J., Vnučko, I., 2012. Approximate all nearest neighbor search for high dimensional entropy estimation for image registration. Signal Processing 92, 1302–1316.

Lange, T., Wenckebach, T., Lamecker, H., Seebass, M., Hünerbein, M., Eulenstein, S., Gebauer, B., Schlag, P., 2005a. Registration of different phases of contrast enhanced CT/MRI data for computer assisted liver surgery planning: evaluation of state of the art methods. The International Journal of Medical Robotics and Computer Assisted Surgery 1, 6–20.

Lange, T., Wenckebach, T., Lamecker, H., Seebass, M., Hunerbein, M., Eulenstein, S., Schlag, P.M., 2005b. Registration of portal and hepatic venous phase of MR/CT data for computer-assisted liver surgery planning. CARS: Computer Assisted Radiology and Surgery 1281, 768–772.

Ledesma-Carbayo, M.J., Kybic, J., Desco, M., Santos, A., Suhling, M., Hunziker, P., Unser, M., 2005. Spatio-temporal nonrigid registration for ultrasound cardiac motion estimation. IEEE Transactions on Medical Imaging 24, 1113–1126.

Lee, W.C.C., Tublin, M.E., Chapman, B.E., 2005. Registration of MR and CT images of the liver: comparison of voxel similarity and surface based registration algorithms. Computer Methods and Programs in Biomedicine 78, 101–114.

Loeckx, D., Slagmolen, P., Maes, F., Vandermeulen, D., Suetens, P., 2010. Nonrigid image registration using conditional mutual information. IEEE Transactions on Medical Imaging 29, 19–29.

Lu, C., Chelikani, S., Papademetris, X., Knisely, J.P., Milosevic, M.F., Chen, Z., Jaffray, D.A., Staib, L.H., Duncan, J.S., 2011. An integrated approach to segmentation and nonrigid registration for application in image-guided pelvic radiotherapy. Medical Image Analysis 15, 772–785.

Maes, F., Collignon, A., Vandermeulen, D., Marchal, G., Suetens, P., 1997. Multimodality image registration by maximization of mutual information. IEEE Transactions on Medical Imaging 16, 187–198.

Maintz, J., Viergever, M.A., 1998. A survey of medical image registration. Medical Image Analysis 2, 1–36.

Mattes, D., Haynor, D.R., Vesselle, H., Lewellyn, T.K., Eubank, W., 2001. Nonrigid multimodality image registration. In: SPIE, pp. 1609–1620.

Mattes, D., Haynor, D.R., Vesselle, H., Lewellen, T.K., Eubank, W., 2003. PET-CT image registration in the chest using free-form deformations. IEEE Transactions on Medical Imaging 22, 120–128.

Oguro, S., Tokuda, J., Elhawary, H., Haker, S., Kikinis, R., Tempany, C., Hata, N., 2009. MRI signal intensity based B-Spline nonrigid registration for pre-and intraoperative imaging during prostate brachytherapy. Journal of Magnetic Resonance Imaging 30, 1052–1058.

Oliva, M.R., Saini, S., 2004. Liver cancer imaging: role of CT, MRI, US and PET. Cancer Imaging 4, S42.

Oudkerk, M., Torres, C.G., Song, B., König, M., Grimm, J., Fernandez-Cuadrado, J., Op de Beeck, B., Marquardt, M., van Dijk, P., de Groot, J.C., 2002. Characterization of liver lesions with Mangafodipir Trisodium-enhanced MR imaging: multicenter study comparing MR and dual-phase spiral CT1. Radiology 223, 517.

Park, S.B., Rhee, F.C., Monroe, J.I., Sohn, J.W., 2010. Spatially weighted mutual information image registration for image guided radiation therapy. Medical Physics 37, 4590–4601.

Pluim, J., Maintz, J., Viergever, M., 2000a. Image registration by maximization of combined mutual information and gradient information. In: Medical Image Computing and Computer-Assisted Intervention – MICCAI. Springer, pp. 103–129.

Pluim, J., Maintz, J., Viergever, M., 2000b. Image registration by maximization of combined mutual information and gradient information. IEEE Transactions on Medical Imaging 19, 809.

Pluim, J.P.W., Maintz, J.B.A., Viergever, M.A., 2003. Mutual-information-based registration of medical images: a survey. IEEE Transactions on Medical Imaging 22, 986–1004.

Radtke, A., Nadalin, S., Sotiropoulos, G.C., Molmenti, E.P., Schroeder, T., Valentin-Gamazo, C., Lang, H., Bockhorn, M., Peitgen, H.O., Broelsch, C.E., Malago, M., 2007. Computer-assisted operative planning in adult living donor liver transplantation: a new way to resolve the dilemma of the middle hepatic vein. World Journal of Surgery 31, 175–185.

Rodriguez-Carranza, C.E., Loew, M.H., 1999. Global optimization of weighted mutual information for multi-modality image registration. In: Proc. SPIE, pp. 89–96.

Rogelj, P., Kovačič, S., Gee, J.C., 2003. Point similarity measures for non-rigid registration of multi-modal data. Computer Vision and Image Understanding 92, 112–140.

Rohlfing, T., Maurer Jr. C.R., O'Dell, W.G., Zhong, J., 2001. Modeling liver motion and deformation during the respiratory cycle using intensity-based free-form registration of gated MR images. In: Proc. Visualization, Display, and Image-guided Procedures, pp. 337–348.

Rueckert, D., Schnabel, J.A., 2011. Medical image registration. Biomedical Image Processing, 131–154.

Rueckert, D., Sonoda, L.I., Hayes, C., Hill, D.L.G., Leach, M.O., Hawkes, D.J., 1999. Nonrigid registration using free-form deformations: application to breast MR images. IEEE Transactions on Medical Imaging 18, 712–721.

Rueckert, D., Clarkson, M., Hill, D., Hawkes, D., 2000. Non-rigid registration using higher-order mutual information. In: Proc SPIE, pp. 438–447.

Russakoff, D., Tomasi, C., Rohlfing, T., Maurer, C., 2004. Image similarity using mutual information of regions. Computer Vision-ECCV, pp. 596–607.

Schnabel, J., Rueckert, D., Quist, M., Blackall, J., Castellano-Smith, A., Hartkens, T., Penney, G., Hall, W., Liu, H., Truwit, C., 2001. A generic framework for non-rigid registration based on non-uniform multi-level free-form deformations. In: Proc. International Conference on Medical Image Computing and Computer-Assisted Intervention MICCAI. Springer, pp. 573–581.

Solbiati, L., Cova, L., Ierace, T., Marelli, P., Dellanoce, M., 1999. Liver cancer imaging: the need for accurate detection of intrahepatic disease spread. Journal of Computer Assisted Tomography 23, S29–S37.

Studholme, C., Hill, D., Hawkes, D., 1996. Incorporating connected region labelling into automatic image registration using mutual information. Workshop on Mathematical Methods in Biomedical Image Analysis, pp. 23–31.

Studholme, C., Drapaca, C., Iordanova, B., Cardenas, V., 2006. Deformation-based mapping of volume change from serial brain MRI in the presence of local tissue contrast change. IEEE Transactions on Medical Imaging 25, 626–639.

Tan, J., Lim Joon, D., Fitt, G., Wada, M., Lim Joon, M., Mercuri, A., Marr, M., Chao, M., Khoo, V., 2010. The utility of multimodality imaging with CT and MRI in defining rectal tumour volumes for radiotherapy treatment planning: a pilot study. Journal of Medical Imaging and Radiation Oncology 54, 562–568.

Thévenaz, P., Unser, M., 1996. A pyramid approach to sub-pixel image fusion based on mutual information. In: Int. Conference on Image Processing, vol. 261. IEEE, pp. 265–268.

Thévenaz, P., Unser, M., 2000. Optimization of mutual information for multiresolution image registration. IEEE Transactions on Image Processing 9, 2083–2099.

Thévenaz, P., Ruttimann, U.E., Unser, M., 1998. A pyramid approach to subpixel registration based on intensity. IEEE Transactions on Image Processing 7, 27–41.

Thorwarth, D., Müller, A.-C., Pfannenberg, C., Beyer, T., 2013. Combined PET/MR Imaging Using 68Ga-DOTATOC for Radiotherapy Treatment Planning in Meningioma Patients, Theranostics, Gallium-68, and Other Radionuclides. Springer, pp. 425–439.
Tohka, J., Zijdenbos, A., Evans, A., 2004. Fast and robust parameter estimation for statistical partial volume models in brain MRI. NeuroImage 23, 84–97.
Unser, M., 1999. Splines: a perfect fit for signal and image processing. IEEE Signal Processing Magazine 16, 22–38.
Unser, M., Aldroubi, A., Eden, M., 1993. The L2-polynomial spline pyramid. IEEE Transactions on Pattern Analysis and Machine Intelligence 15, 364–379.
Van Dalen, J., Vogel, W., Huisman, H., Oyen, W., Jager, G., Karssemeijer, N., 2004. Accuracy of rigid CT–FDG-PET image registration of the liver. Physics in Medicine and Biology 49, 5393.
Villard, P.-F., Boshier, P., Bello, F., Gould, D., 2011. Virtual Reality Simulation of Liver Biopsy with a Respiratory Component, Liver Biopsy. InTech, pp. 315–334.
Weinmann, H.J., Ebert, W., Misselwitz, B., Schmitt-Willich, H., 2003. Tissue-specific MR contrast agents. European Journal of Radiology 46, 33–44.
Wells III, W.M., Viola, P., Atsumi, H., Nakajima, S., Kikinis, R., 1996. Multi-modal volume registration by maximization of mutual information. Medical Image Analysis 1, 35–51.
Yi, Z., Soatto, S., 2011. Multimodal registration via spatial-context mutual information. In: Lecture Notes in Computer Science, IPMI. Springer, pp. 424–435.
Zhuang, X., Arridge, S., Hawkes, D.J., Ourselin, S., 2011. A nonrigid registration framework using spatially encoded mutual information and free-form deformations. IEEE Transactions on Medical Imaging 30, 1819–1828.
Zitova, B., Flusser, J., 2003. Image registration methods: a survey. Image and Vision Computing 21, 977–1000.